



# Electrostatic Field Formed by Charge Separation in Antiparallel Magnetic Reconnection

Shihang Hu<sup>1</sup> , Quanming Lu<sup>1,2,3</sup> , Yukang Shu<sup>1</sup> , San Lu<sup>1,2,3</sup> , Kai Huang<sup>1</sup> , and Jia Nan<sup>1</sup> <sup>1</sup> CAS Key Lab of Geospace Environment, School of Earth and Space Sciences, University of Science and Technology of China, Hefei 230026, People's Republic of China; [qmlu@ustc.edu.cn](mailto:qmlu@ustc.edu.cn)<sup>2</sup> Deep Space Exploration Laboratory, CAS Center for Excellence in Comparative Planetology, Hefei 230026, People's Republic of China<sup>3</sup> Collaborative Innovation Center of Astronautical Science and Technology, Harbin, People's Republic of China

Received 2024 November 17; revised 2025 April 21; accepted 2025 May 7; published 2025 June 5

## Abstract

The Hall effect resulting from the decoupled motions between ions and electrons is a critical factor in modeling collisionless magnetic reconnection. It leads to the production of charge separation in the reconnection plane, generating the electrostatic field with components perpendicular and parallel to the magnetic field. In this paper, using a 2.5-dimensional particle-in-cell simulation, we investigate the formation of the charge separation in antiparallel magnetic reconnection. The charge separation is formed in three regions: the electron inflow region and the dipolarization front (DF) region both exhibit a positive charge density, while the electron outflow region exhibits a negative charge density. These charge separations generate the Hall electric field perpendicular to the magnetic field and the parallel electrostatic field. We quantitatively analyze the effects of the magnetic flux tube's geometric dimensions and the parallel electron flux on the formation of charge separation. In the electron inflow region, the parallel electron flux from regions with smaller cross sections to regions with larger cross sections reduces electron density, generating a positive charge density near the separatrix. In contrast, within the outflow region, the parallel electron flux from regions with larger cross sections to regions with smaller cross sections increases electron density, generating a negative charge density near the separatrix. Besides, we attribute the charge separation in the DF region mainly to the acceleration of electrons, which generates a sharply varying parallel electron flux. This drives a net outflow of electrons and establishes an accumulation of positive charge.

*Unified Astronomy Thesaurus concepts:* Space plasmas (1544); Plasma physics (2089); Planetary magnetospheres (997)

## 1. Introduction

Magnetic reconnection is a plasma process that converts magnetic energy to particle energy via changes in magnetic field line topologies (V. M. Vasyliunas 1975; D. Biskamp 2000; M. Yamada et al. 2010; S. Wang & Q. Lu 2019). It is widely believed that magnetic reconnection energizes particles and causes explosive phenomena in various plasma environments, ranging from solar atmosphere (S. Masuda et al. 1994; S. Krucker et al. 2010; P. A. Cassak & M. A. Shay 2012) and interplanetary space (F. Wei et al. 2003; J. T. Gosling et al. 2005; R. Wang et al. 2023a, 2023b) to the planet's magnetosphere (M. Øieroset et al. 2001; R. Wang et al. 2010; T. L. Zhang et al. 2012; Q. Lu et al. 2022; R. Wang et al. 2024), as well as in laboratory experiments (M. Yamada et al. 2006; J. Egedal et al. 2007; C. K. Li et al. 2007; Q.-L. Dong et al. 2012; M. Yamada et al. 2015; L. Sang et al. 2022). In the collisionless magnetic reconnection model, the diffusion region has two substructures: the ion diffusion region (IDR) and the electron diffusion region (EDR; Z. W. Ma & A. Bhattacharjee 2001; P. L. Pritchett 2001; Q. Lu et al. 2010; M. Zhou et al. 2019). In the IDR with the scale size on the order of the ion inertial length, the electrons are magnetized, while the ions are demagnetized. In the EDR with the scale size on the order of the electron inertial length, which is embedded in the IDR, the electron motions also

become demagnetized (P. L. Pritchett 2001; Q. Lu et al. 2010, 2011).

The Hall effect resulting from the decoupled motions between ions and electrons is a critical factor in modeling collisionless magnetic reconnection (J. Birn et al. 2001; Z. W. Ma & A. Bhattacharjee 2001; Q. Lu et al. 2010, 2011), and it leads to the production of Hall current and charge separation in the reconnection plane (M. A. Shay et al. 2001; Q. Lu et al. 2010, 2011). The in-plane Hall current generates the characteristic quadrupolar structure of the out-of-plane magnetic field (C. Huang et al. 2010; Q. Lu et al. 2010, 2011), while the charge separation can cause the electrostatic field (J. R. Wygant et al. 2005; M. V. Goldman et al. 2016; S. Lu et al. 2021). This electrostatic field consists of the components perpendicular and parallel to the magnetic field. The former is called the Hall electric field (J. R. Wygant et al. 2005; J. F. Drake et al. 2008; M. V. Goldman et al. 2016), and the latter makes a significant contribution to the parallel electric field (J. Egedal et al. 2015; C. Huang et al. 2015; S. Lu et al. 2021).

J. Egedal et al. (2015) proposed a mechanism to explain the formation of charge separation in the electron inflow region during antiparallel magnetic reconnection. They considered a flux tube within the IDR but outside the EDR, where the ions are demagnetized and the electrons are magnetized. During the reconnection process, the flux tube within the inflow region expands because of the weakening magnetic field strength. Within the IDR, the ions are demagnetized with a nearly uniform density. Therefore, the expanding flux tube will encompass an increased number of ions. Meanwhile, the electrons are frozen, and charge separation will be caused

when the parallel electron flux  $n_e V_{e\parallel}$  fails to supply sufficient electrons. This charge separation, located in the density cavity, generates a strong double-layer electric field. A threshold  $\beta_{e\infty} < \sqrt{m_e/m_i}$  ( $\beta_{e\infty} = 2\mu_0 p_{e\infty}/B_\infty^2$  is the ratio of the background electron pressure to the magnetic pressure) for developing the strong double-layer electric field is also given in J. Egedal et al. (2015). This structure has already been observed in the separatrix region during magnetotail reconnection by Cluster (R. Wang et al. 2013, 2014).

In this paper, we demonstrate that the Hall effect not only induces charge separation in the electron inflow region but also drives significant charge separation within the electron outflow region and the dipolarization front (DF) region during antiparallel magnetic reconnection. Furthermore, we quantitatively analyze the formation of these charge separation processes.

## 2. Simulation Model

A 2.5-dimensional (2.5D; in the  $x$ - $z$  plane) particle-in-cell (PIC; T. D. Arber et al. 2015) simulation is performed in this paper. The simulation is initialized with a Harris current sheet and a uniform background population. The initial magnetic field is  $\mathbf{B}(z) = B_0 \tanh(z/\delta) \mathbf{e}_x$ , corresponding to an initial magnetic flux  $\Psi(z) = B_0 \delta \ln[\cosh(z/\delta)]$  (magnetic flux function  $\Psi$  satisfies  $B_x = \partial\Psi/\partial z$  and  $B_z = -\partial\Psi/\partial x$ ). We add an initial perturbation  $\Delta\Psi(x, z) = 0.1 B_0 \delta \operatorname{sech}(x/\delta) \operatorname{sech}(z/\delta)$  onto the initial magnetic flux to launch magnetic reconnection at the center of the simulation domain. The initial plasma density is  $n(z) = n_0 \operatorname{sech}^2(z/\delta) + n_\infty$ , where  $n_0$  is the peak density in the Harris current sheet and  $n_\infty$  is the uniform background density. Note that  $d_i$  is the ion inertial length evaluated using  $n_0$ , and  $\delta = 0.5 d_i$  is the current sheet half-thickness. The ion-to-electron mass ratio is  $m_i/m_e = 400$ , and the speed of light is  $c = 40 V_A$ , where  $V_A$  is the Alfvén speed evaluated using  $B_0$  and  $n_0$ . The ion-to-electron temperature ratio of the Harris population is  $T_{i0}/T_{e0} = 5$ , and the temperature ratio for the uniform background population is the same,  $T_{i\infty}/T_{e\infty} = T_{i0}/T_{e0}$ . The grid size is  $\Delta x = \Delta z = 0.025 d_i$ , and the time step is  $\Delta t = 4 \times 10^{-4} \Omega_i^{-1}$ , where  $\Omega_i$  is the ion gyrofrequency evaluated using  $B_0$ . The simulation domain, in the  $x$ - $z$  plane, is  $[-L_x/2, L_x/2] \times [-L_z/2, L_z/2]$ , where  $L_x = 100 d_i$  and  $L_z = 20 d_i$ , and therefore, the grid number is  $N_x \times N_z = 4000 \times 800$ .  $1.28 \times 10^9$  particles for every species employed in the simulation. Periodic boundary conditions are assumed in the  $x$ -direction, while in the  $z$ -direction, conducting boundary conditions are retained and particles are specularly reflected.

In this paper, we run two cases. In Case A, the background plasma density is  $n_\infty = 0.10 n_0$ , and the background electron temperature is  $T_{e\infty}/T_{e0} = 3$ , resulting in a plasma beta  $\beta_{e\infty} = 2\mu_0 n_\infty k_B T_{e\infty}/B_0^2 = 0.050$ . In Case B, the background plasma density is  $n_\infty = 0.05 n_0$ , and the background electron temperature is  $T_{e\infty}/T_{e0} = 1/3$ , resulting in a plasma beta  $\beta_{e\infty} = 0.003$ .

## 3. Simulation Results

We plot the temporal evolution of the reconnected magnetic flux  $\Psi$  at the X-line corresponding to Case A and B in Figure 1. The reconnection rate is the time derivative of the reconnected magnetic flux. Obviously, the maximum reconnection rate in Case A is smaller than that in Case B—specifically, it is 0.39 in Case A and 0.59 in Case B. This is consistent with previous

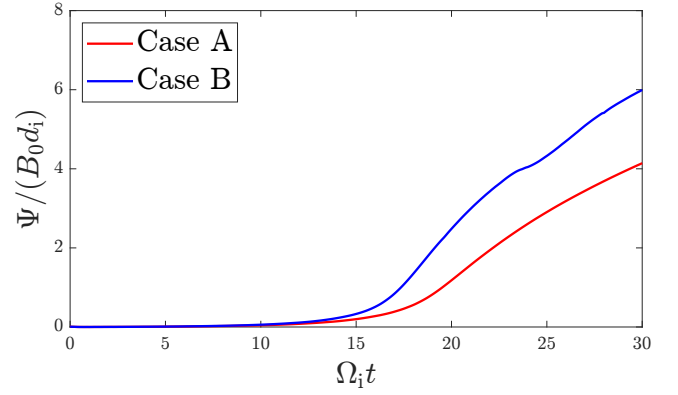


**Figure 1.** The temporal evolution of the reconnected magnetic flux  $\Psi$  at the X-line in Case A and B.

work (P. Wu et al. 2011; S. Lu et al. 2019), showing that the reconnection rate becomes smaller with the increase of  $\beta_{e\infty}$ . In this paper, we will at first describe the results in Case A and then compare two simulation cases.

In order to investigate the evolution of the charge separation and the resulting electrostatic field, Figure 2 shows (a) the electrostatic potential  $\varphi$ , (b) the perpendicular component of electrostatic field  $E_{s\perp}$ , and (c) the parallel component of electrostatic field  $E_{s\parallel}$  at  $\Omega_i t = 20.5, 22.5, 24.5$ , and  $26.5$  in Case A. The electrostatic potential  $\varphi$  is calculated by solving Poisson’s equation, with the zero potential reference set on the upper boundary of the simulation domain. The corresponding electrostatic field is then derived from  $\mathbf{E}_s = -\nabla\varphi$ . The parallel electrostatic field is defined as  $E_{s\parallel} = \mathbf{E}_s \cdot \mathbf{b}$ , where  $\mathbf{b} = \mathbf{B}/B$  is the unit magnetic field vector. The perpendicular electrostatic field is defined as  $E_{s\perp} = \sqrt{E_s^2 - E_{s\parallel}^2} \times \operatorname{sgn}[(\mathbf{E}_s \times \mathbf{B}) \cdot \mathbf{e}_y]$ , where  $\operatorname{sgn}(x)$  is the sign function. During the reconnection process, the inflow region exhibits higher electrostatic potential  $\varphi$  compared to the outflow region, generating the well-documented Hall electric field (J. R. Wygant et al. 2005; M. V. Goldman et al. 2016; S. Lu et al. 2021). This Hall electric field  $E_{s\perp}$  is distributed across the electron inflow region and the electron outflow region near the separatrix. The DF region, characterized by the compressed magnetic field within the outflow region, forms during  $\Omega_i t \approx 22.5$ – $24.5$  and exhibits higher electrostatic potential  $\varphi$  than its ambient plasma. For example, the DF region marked with a white rectangle in Figure 2(a) exhibits a lighter blue color than the outflow region. This potential gradient drives the Hall electric field  $E_{s\perp}$  within the DF region, which has been observed during magnetotail reconnection (A. Runov et al. 2011; H. S. Fu et al. 2012). This Hall electric field  $E_{s\perp}$  develops in conjunction with the DF region, and it is relatively weaker than that near the separatrix. Additionally, the electrostatic field parallel to the magnetic field ( $E_{s\parallel}$ ) is also observed in the electron inflow region, the electron outflow region, and the DF region (the magnetic field lines labeled “L1,” “L2,” and “L3” in Figure 3 facilitate the identification of these three regions). This parallel electrostatic field makes a significant contribution to the parallel electric field, which plays an important role in producing energetic electrons through trapping the electrons accelerated by the reconnection electric field (J. T. Dahlin et al. 2014; C. Huang et al. 2015; H. Wang et al. 2016; S. Lu et al. 2021). The parallel electrostatic field  $E_{s\parallel}$  in the electron inflow region is predominantly concentrated around the X-line vicinity. The parallel electrostatic field  $E_{s\parallel}$  in the electron outflow region

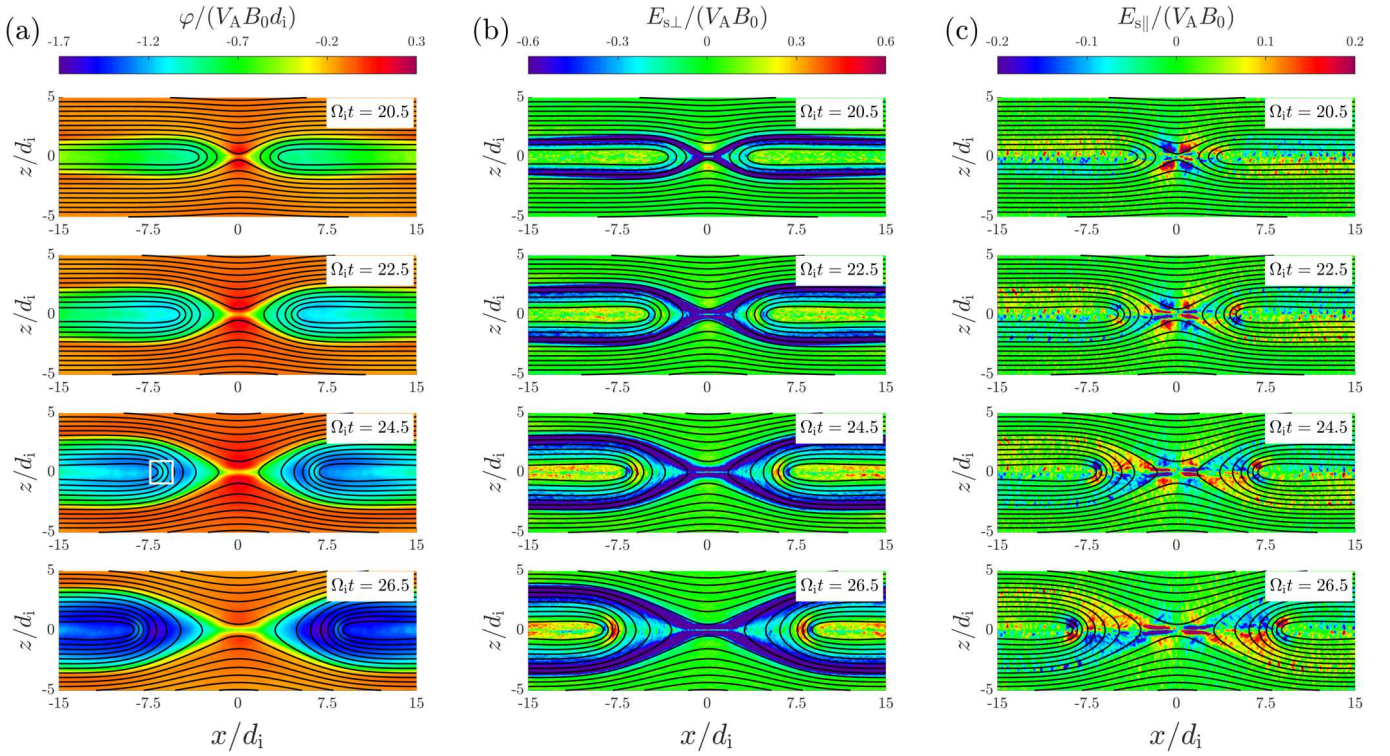


**Figure 2.** Color contours of (a) the electrostatic potential  $\varphi$ , (b) the perpendicular component of electrostatic field  $E_{s\perp}$ , and (c) the parallel component of electrostatic field  $E_{s\parallel}$  at  $\Omega_i t = 20.5, 22.5, 24.5,$  and  $26.5$ . The black lines in the figure represent the magnetic field lines (Case A).

is predominantly distributed between the X-line and the DF region. In comparison with the inflow and outflow regions, the DF region exhibits a relatively stronger parallel electrostatic field  $E_{s\parallel}$ . Furthermore, Figures 2(b)–(c) demonstrate that during the antiparallel magnetic reconnection, the perpendicular component of electrostatic field ( $E_{s\perp} \gtrsim 0.6 V_A B_0$ ) significantly exceeds its parallel component ( $E_{s\parallel} \approx 0.2 V_A B_0$ ).

For a closer view of the charge separation, Figure 3 shows (a) the charge density  $\rho$ , (b) the electrostatic potential  $\varphi$ , (c) the perpendicular component of electrostatic field  $E_{s\perp}$ , and (d) the parallel component of electrostatic field  $E_{s\parallel}$  at  $\Omega_i t = 24.5$ . The magnetic field lines labeled “L1,” “L2,” and “L3” in Figure 3 pass through the electron inflow region, the electron outflow region, and the DF region, respectively. The charge separation is formed in three regions: the electron inflow region and the DF region both exhibit a positive charge density, while the electron outflow region exhibits a negative charge density. The positive charge density in the electron inflow region and the DF region leads to a higher electrostatic potential  $\varphi$ , while the negative charge density in the electron outflow region leads to a lower electrostatic potential  $\varphi$ . As mentioned above, the gradient of these electrostatic potentials  $\varphi$  generates the Hall electric field  $E_{s\perp}$  perpendicular to the magnetic field and the parallel electrostatic field  $E_{s\parallel}$ . The spatial distribution of the Hall electric field is shown in Figure 3(c), and the arrows indicate the direction of  $E_{s\perp}$ . In the separatrix region, the Hall electric field is directed from the electron inflow region to the electron outflow region, matching the orientation of potential drop. Similarly, in the DF region, the direction of the Hall electric field indicated by two arrows matches the orientation of potential drop. The spatial distribution of the parallel electrostatic field is shown in Figure 3(d), with an arrow indicating the unit magnetic field vector  $\mathbf{b}$ . To demonstrate the

codirectionality of the parallel electrostatic field and potential drop, Figure 4 plots the electrostatic potential  $\varphi$  (blue) and the parallel electrostatic field  $E_{s\parallel}$  (red) along the magnetic field lines (a) “L1,” (b) “L2,” and (c) “L3.” In the region between  $x/d_1 = -2.2$  and  $x/d_1 = -0.1$ , along the magnetic field line “L1” passing through the electron inflow region, the electrostatic potential  $\varphi$  increases with negative parallel electrostatic field  $E_{s\parallel}$ . Along the magnetic field line “L2” passing through the electron outflow region, the electrostatic potential  $\varphi$  decreases with positive parallel electrostatic field  $E_{s\parallel}$ . In the region between  $x/d_1 = -8.0$  and  $x/d_1 = -6.3$ , along the magnetic field line “L3” passing through the DF region, the electrostatic potential  $\varphi$  increases with negative parallel electrostatic field  $E_{s\parallel}$ .

In order to explain the formation of charge separation in the collisionless magnetic reconnection, we introduce an equation to describe the change in electron density  $n_e$  during the motion of magnetic flux tube as follows:

$$\begin{aligned} D_{\perp} n_e = & \frac{n_e}{B} D_{\perp} B + n_e (\mathbf{b} \cdot \nabla \mathbf{b}) \cdot \mathbf{V}_{e\perp} \\ & - \mathbf{b} \cdot \nabla (n_e V_{e\parallel}) + \frac{n_e V_{e\parallel}}{B} \mathbf{b} \cdot \nabla B, \end{aligned} \quad (1)$$

where  $(\mathbf{b} \cdot \nabla \mathbf{b})$  is the curvature of the magnetic field and  $D_{\perp} = \left( \frac{\partial}{\partial t} + \mathbf{V}_{e\perp} \cdot \nabla \right)$ . Equation (1) is valid under the ideal electron magnetohydrodynamic condition ( $\mathbf{E} + \mathbf{V}_e \times \mathbf{B} = 0$ ), and the derivation is provided in the Appendix. It should be noted that the bulk velocity of the frozen electrons is decomposed into  $\mathbf{V}_e = V_{e\parallel} \mathbf{b} + \mathbf{V}_{e\perp}$ . Electrons are frozen in to the magnetic flux tube. Therefore, the bulk velocity consists of two components: the parallel component  $V_{e\parallel} \mathbf{b}$  moving along the flux tube and the perpendicular component  $\mathbf{V}_{e\perp}$  moving

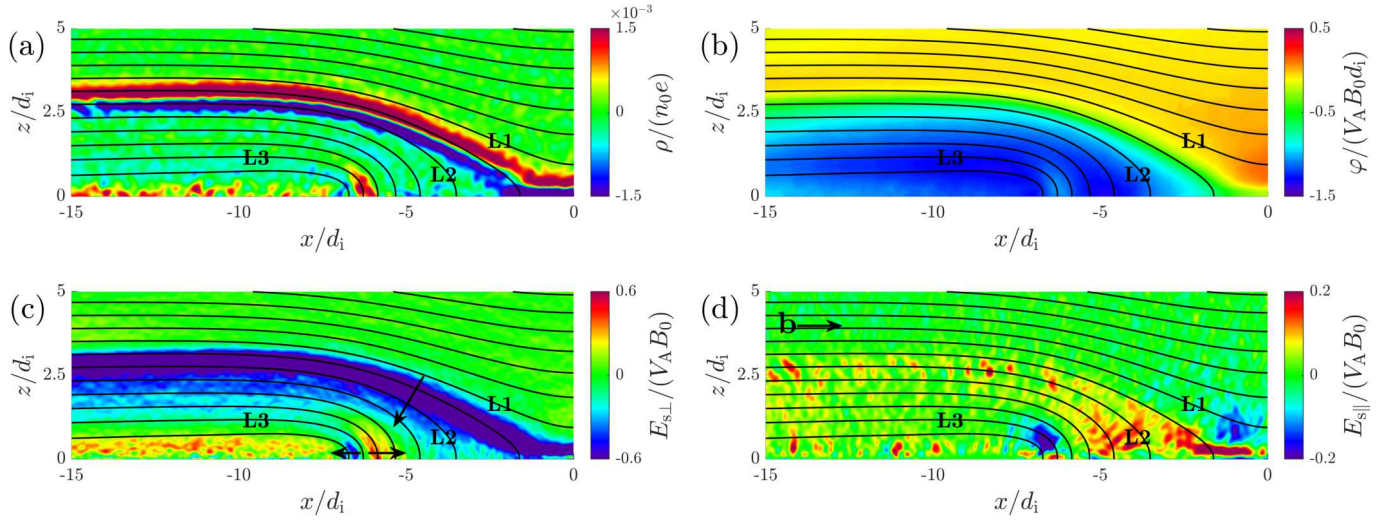


**Figure 3.** Color contours of (a) the charge density  $\rho$ , (b) the electrostatic potential  $\varphi$ , (c) the perpendicular component of electrostatic field  $E_{s\perp}$ , and (d) the parallel component of electrostatic field  $E_{s\parallel}$  at  $\Omega_i t = 24.5$ . The magnetic field lines labeled “L1,” “L2,” and “L3” pass through the electron inflow region, the electron outflow region, and the DF region, respectively. In subgraph (c), the arrows indicate the direction of  $E_{s\perp}$ . In subgraph (d), the arrow indicates the direction of  $\mathbf{b}$ . The black lines in the figure represent the magnetic field lines (Case A).

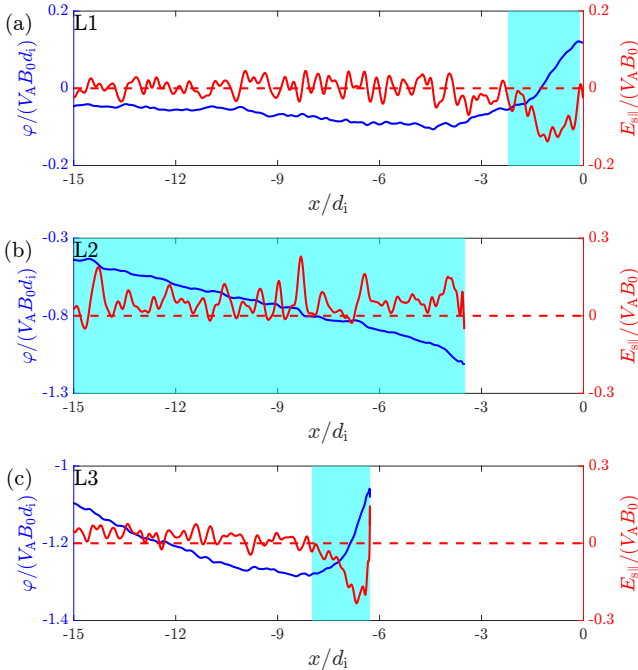


**Figure 4.** The electrostatic potential  $\varphi$  (blue) and the parallel component of electrostatic field  $E_{s\parallel}$  (red) along the magnetic field lines (a) “L1,” (b) “L2,” and (c) “L3” in Figure 3.

with the flux tube. Consequently, the flux tube has a velocity  $\mathbf{V}_{e\perp}$ , and its material derivative is  $D_{\perp} = \left( \frac{\partial}{\partial t} + \mathbf{V}_{e\perp} \cdot \nabla \right)$ .

The physical interpretation of each term in Equation (1) is elucidated by Figure 5. The term on the left side of Equation (1),  $D_{\perp} n_e$ , describes the change in electron density  $n_e$  during the motion of the flux tube. The first and second terms on the right side of Equation (1) quantify the variation of electron density  $n_e$  due to the geometric dimensions of the flux tube, while the third and fourth terms quantify the contribution of the parallel electron flux  $n_e V_{e\parallel}$ . The first term  $\frac{n_e}{B} D_{\perp} B$  quantifies the variation of electron density  $n_e$  due to the cross-sectional area of the flux tube. Specifically, the cross-sectional

area of the flux tube decreases as the magnetic field intensifies ( $D_{\perp} B > 0$ ; see Figure 5(a)), leading to an increase in electron density  $n_e$ . The second term  $n_e (\mathbf{b} \cdot \nabla \mathbf{b}) \cdot \mathbf{V}_{e\perp}$  quantifies the variation of electron density  $n_e$  due to the length of the flux tube. When the flux tube moves along its curvature, such that  $(\mathbf{b} \cdot \nabla \mathbf{b}) \cdot \mathbf{V}_{e\perp} > 0$ , the length of the flux tube decreases (see Figure 5(b)), leading to an increase in electron density  $n_e$ . The third term  $-\mathbf{b} \cdot \nabla (n_e V_{e\parallel})$  quantifies the variation of electron density  $n_e$  due to the net inflow or outflow of the parallel electron flux (see Figure 5(c)). This term can also be expressed as  $-\partial(n_e V_{e\parallel})/\partial s$ , where  $s$  denotes the path along the magnetic field line. The parallel electron flux also contributes to the variation of electron density  $n_e$  through an additional mechanism, which is described by the fourth term  $\frac{n_e V_{e\parallel}}{B} \mathbf{b} \cdot \nabla B$ . When  $\frac{n_e V_{e\parallel}}{B} \mathbf{b} \cdot \nabla B > 0$ , electrons flow within the same flux tube from regions with larger cross sections to regions with smaller cross sections (see Figure 5(d)), leading to an increase in electron density  $n_e$ .

In order to explain the formation of charge separation using Equation (1), Figure 6 shows (a) the nonideal electric field  $R_{iy}$ , (b) the nonideal electric field  $R_{ey}$ , (c)  $\frac{n_e}{B} D_{\perp} B + n_e (\mathbf{b} \cdot \nabla \mathbf{b}) \cdot \mathbf{V}_{e\perp}$ , (d)  $-\mathbf{b} \cdot \nabla (n_e V_{e\parallel})$ , (e)  $\frac{n_e V_{e\parallel}}{B} \mathbf{b} \cdot \nabla B$ , and (f)  $D_{\perp} n_e$  at  $\Omega_i t = 24.5$ . The nonideal electric fields in the ion and electron frames  $\mathbf{R}_{i,e} = \mathbf{E} + \mathbf{V}_{i,e} \times \mathbf{B}$  are introduced to identify the IDR and EDR. Figure 6(a) shows the IDR’s spatial profile with  $R_{iy} \neq 0$ , a signature of ion demagnetization. Similarly, Figure 6(b) shows the EDR’s spatial profile with  $R_{ey} \neq 0$ , a signature of electron demagnetization. A multiscale structure of the inner and outer EDRs can be observed (H. Karimabadi et al. 2007). We consider a flux tube within the IDR but outside the EDR, where the ions are demagnetized and the electrons are magnetized. First we investigate the formation of charge separation in the inflow region through Figures 6(c)–(f). It is clear that the flux tube in the inflow region expands as it moves into the X-line, where  $\left[ \frac{n_e}{B} D_{\perp} B + n_e (\mathbf{b} \cdot \nabla \mathbf{b}) \cdot \mathbf{V}_{e\perp} \right] < 0$ , which contributes to a decrease in electron density  $n_e$ . To balance the decrease in electron density  $n_e$ , the parallel electron flux generates a net inflow of electrons, where  $-\mathbf{b} \cdot \nabla (n_e V_{e\parallel}) > 0$ . In this process, the electrons flow into the diffusion region along the

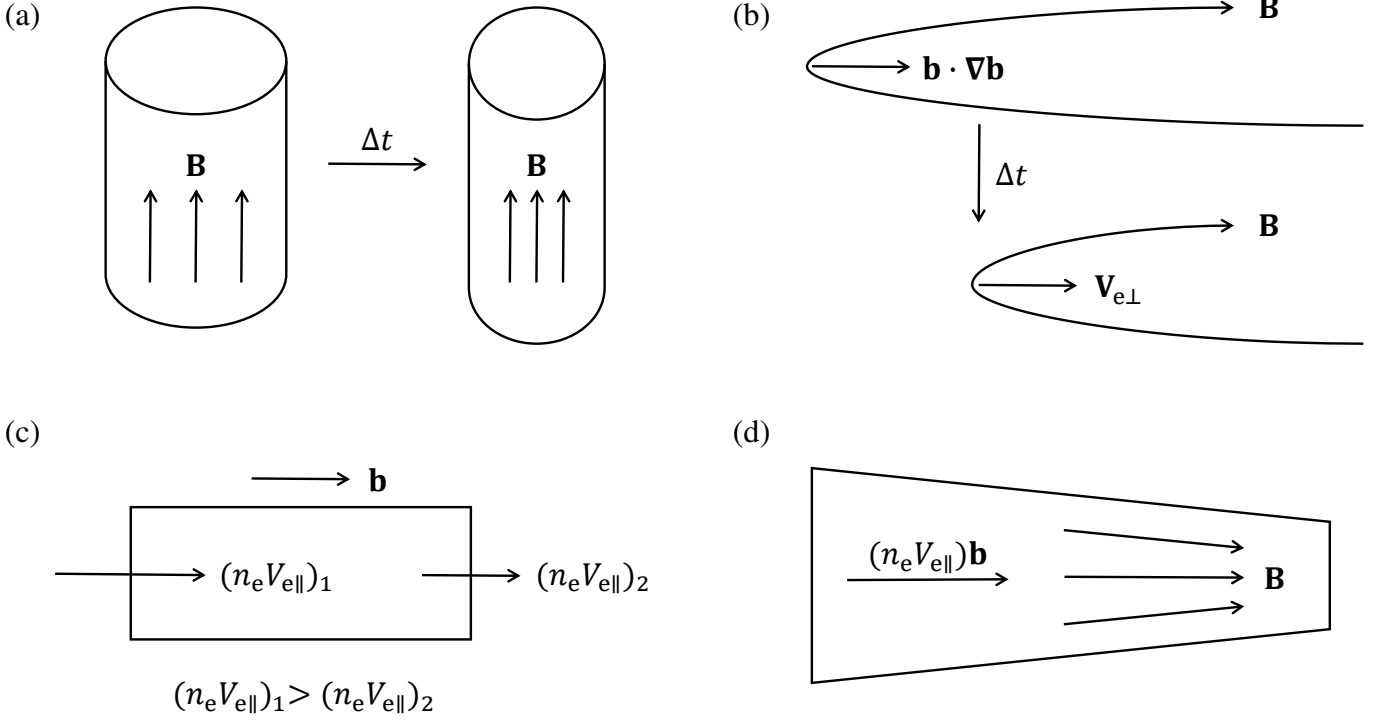


**Figure 5.** A conceptual diagram illustrating the physical interpretation of each term on the right side of Equation (1). (a)  $D_{\perp}B > 0$ , (b)  $(\mathbf{b} \cdot \nabla \mathbf{b}) \cdot \mathbf{V}_{e\perp} > 0$ , (c)  $-\mathbf{b} \cdot \nabla(n_e V_{e\parallel}) > 0$ , and (d)  $\frac{n_e V_{e\parallel}}{B} \cdot \nabla B > 0$ .

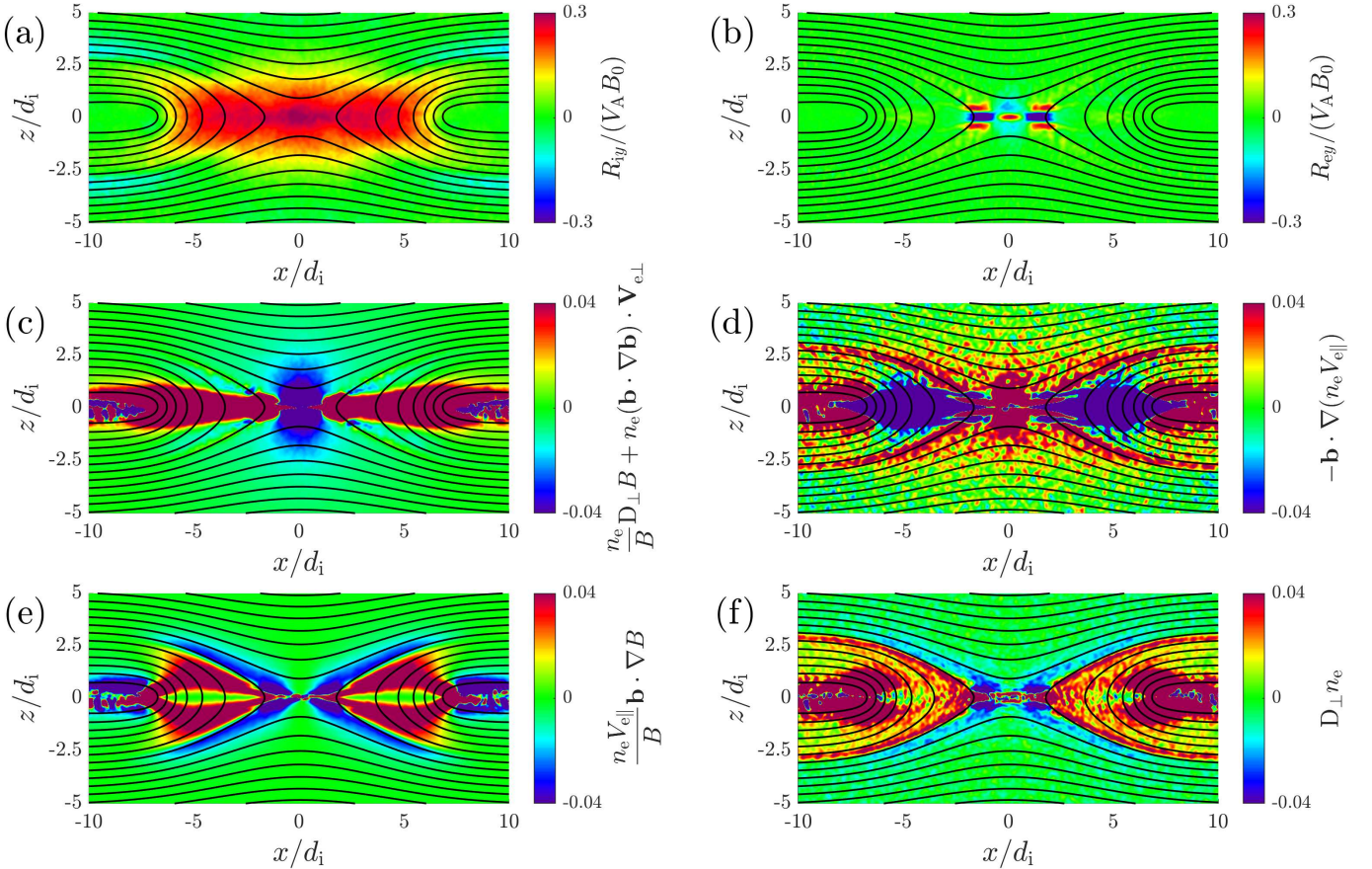


**Figure 6.** Color contours of (a) the nonideal electric field  $R_{xy}$ , (b) the nonideal electric field  $R_{ey}$ , (c)  $\frac{n_e}{B} D_{\perp} B + n_e (\mathbf{b} \cdot \nabla \mathbf{b}) \cdot \mathbf{V}_{e\perp}$ , (d)  $-\mathbf{b} \cdot \nabla(n_e V_{e\parallel})$ , (e)  $\frac{n_e V_{e\parallel}}{B} \cdot \nabla B$ , and (f)  $D_{\perp} n_e$  at  $\Omega_i t = 24.5$ . The black lines in the figure represent the magnetic field lines (Case A).

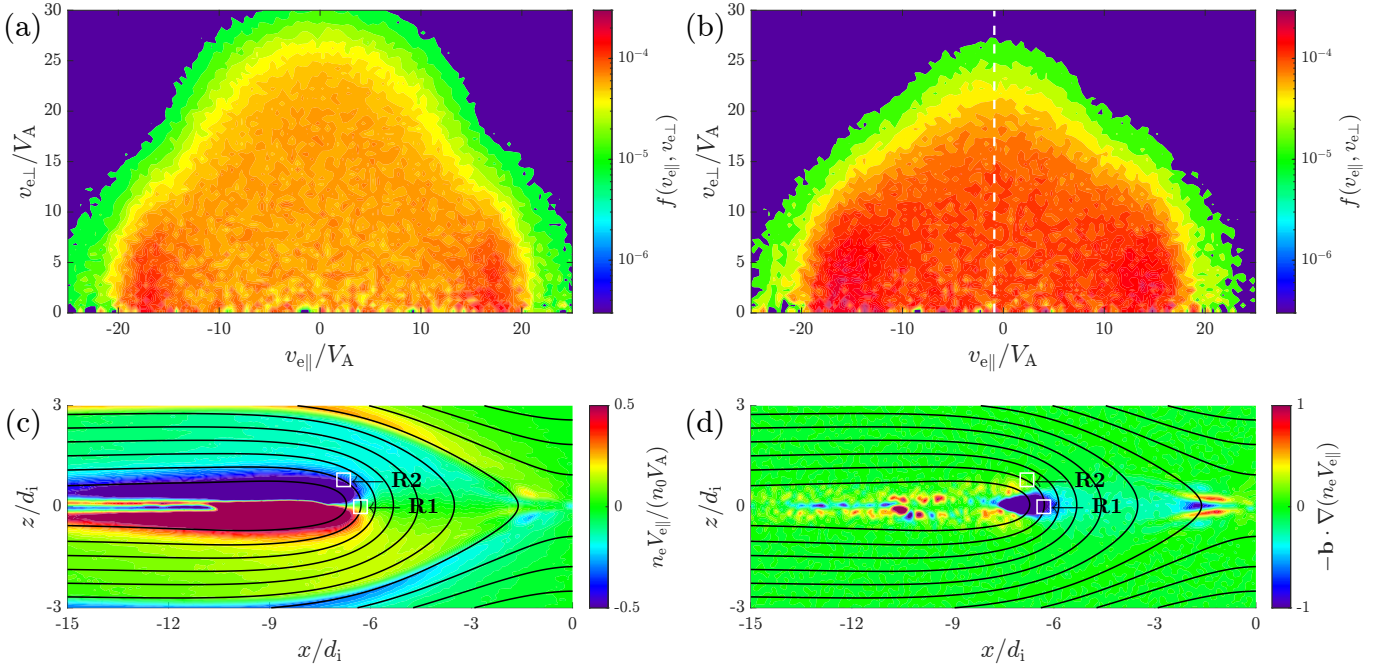


**Figure 7.** (a) and (b) display the velocity distribution of electrons  $f(v_{\parallel}, v_{\perp})$  within the spatial regions marked with rectangles “R1” and “R2,” which are labeled in subgraphs (c)–(d). The white dashed line in subgraph (b) represents  $v_{\parallel}/V_A = -0.9$ . The spatial domains of rectangles “R1” and “R2” are defined as  $(-6.5d_i, -6.1d_i) \times (-0.2d_i, 0.2d_i)$  and  $(-7.0d_i, -6.6d_i) \times (0.6d_i, 1.0d_i)$ . (c) and (d) display the color contours of the parallel electron flux  $n_e V_{e\parallel}$  and  $-\mathbf{b} \cdot \nabla(n_e V_{e\parallel})$  at  $\Omega_i t = 24.5$ . The black lines in subgraphs (c)–(d) represent the magnetic field lines (Case A).

flux tube, from regions with smaller cross sections to regions with larger cross sections, such that  $\frac{n_e V_{e\parallel}}{B} \mathbf{b} \cdot \nabla B < 0$ , which contributes to a decrease in electron density  $n_e$  near the separatrix. Consequently, the electron density  $n_e$  decreases ( $D_{\perp} n_e < 0$ ) in the inflow region near the separatrix, where a positive charge density is observed, as shown in Figure 3(a). Then we investigate the formation of charge separation in the outflow region through Figures 6(c)–(f). In contrast to the inflow region, the flux tube in the outflow region shrinks as it moves away from the X-line, where  $\left[ \frac{n_e}{B} D_{\perp} B + n_e (\mathbf{b} \cdot \nabla \mathbf{b}) \cdot \mathbf{V}_{e\perp} \right] > 0$ , which contributes to an increase in electron density  $n_e$ . To suppress the increase in electron density  $n_e$ , the parallel electron flux generates a net outflow of electrons, where  $-\mathbf{b} \cdot \nabla(n_e V_{e\parallel}) < 0$ . In this process, the electrons flow away from the diffusion region along the flux tube, from regions with larger cross sections to regions with smaller cross sections, such that  $\frac{n_e V_{e\parallel}}{B} \mathbf{b} \cdot \nabla B > 0$ , which contributes to an increase in electron density  $n_e$  near the separatrix. Consequently, the electron density  $n_e$  increases ( $D_{\perp} n_e > 0$ ) in the outflow region near the separatrix, where a negative charge density is observed, as shown in Figure 3(a). Therefore, in both the electron inflow and outflow regions, the term  $\frac{n_e V_{e\parallel}}{B} \mathbf{b} \cdot \nabla B$  in Equation (1) is responsible for the charge separation near the separatrix.

The formation of charge separation in the DF region can be illustrated by Figure 7. Figures 7(a)–(b) display the velocity distribution of electrons  $f(v_{\parallel}, v_{\perp})$  within the spatial regions marked with rectangles “R1” and “R2,” which are labeled in Figures 7(c)–(d). The spatial domains of rectangles “R1” and “R2” are defined as  $(-6.5d_i, -6.1d_i) \times (-0.2d_i, 0.2d_i)$  and  $(-7.0d_i, -6.6d_i) \times (0.6d_i, 1.0d_i)$ . Figures 7(c)–(d) display the parallel electron flux  $n_e V_{e\parallel}$  and  $-\mathbf{b} \cdot \nabla(n_e V_{e\parallel})$  at  $\Omega_i t = 24.5$ . The velocity distributions in the selected regions near the DF show that the electrons with pitch angles around  $90^\circ$  are energized by betatron acceleration, and the electrons with pitch

angles around  $0^\circ$  and  $180^\circ$  are energized by Fermi acceleration (H. S. Fu et al. 2011, 2013; M. Wu et al. 2013; C. Huang et al. 2015; S. Lu et al. 2016; K. Huang et al. 2021; Z. Wang et al. 2023). When leaving away from the center of the DF, these distributions become asymmetric: in the rectangle “R2,” these electrons exhibit an average velocity  $\bar{v}_{e\parallel} = -0.9V_A$  (the white dashed line) in the parallel direction, which leads to an electron outflow  $n_e V_{e\parallel}$  from the DF region. Therefore, as shown in Figure 7(c), when magnetic field lines pass through the DF region, the parallel electron flux  $n_e V_{e\parallel}$  sharply varies. Figure 7(d) further confirms that electrons in the DF region exhibit  $-\mathbf{b} \cdot \nabla(n_e V_{e\parallel}) < 0$ . Ultimately, this pronounced  $-\mathbf{b} \cdot \nabla(n_e V_{e\parallel})$  drives a net outflow of electrons and establishes an accumulation of positive charge.

Here we contrast the simulation results of Case B against Case A. Figure 8 shows (a) the electrostatic potential  $\varphi$ , (b) the perpendicular component of electrostatic field  $E_{s\perp}$ , (c) the parallel component of electrostatic field  $E_{s\parallel}$ , (d)  $\frac{n_e}{B} D_{\perp} B + n_e (\mathbf{b} \cdot \nabla \mathbf{b}) \cdot \mathbf{V}_{e\perp}$ , (e)  $-\mathbf{b} \cdot \nabla(n_e V_{e\parallel})$ , and (f)  $\frac{n_e V_{e\parallel}}{B} \mathbf{b} \cdot \nabla B$  at  $\Omega_i t = 22.0$  in Case B. In this case, the spatial structure of the electrostatic potential  $\varphi$  does not show significant differences compared to Case A. The spatial structures of terms in Equation (1),  $\frac{n_e}{B} D_{\perp} B + n_e (\mathbf{b} \cdot \nabla \mathbf{b}) \cdot \mathbf{V}_{e\perp}$  and  $\frac{n_e V_{e\parallel}}{B} \mathbf{b} \cdot \nabla B$ , also do not show significant differences compared to Case A. However, the electrostatic field  $\mathbf{E}_s$  exhibits a larger magnitude in both the perpendicular and parallel components. Besides, in the separatrix region in Figure 8(c), the electrostatic solitary waves (ESWs) with the alternating appearance of positive and negative parallel electrostatic field  $E_{s\parallel}$  are observed. These ESWs are triggered by the electron two-stream instability, and their evolution has been thoroughly investigated (K. Fujimoto 2014; C. Huang et al. 2014; H. S. Fu et al. 2020; C. Chang et al. 2021). In the separatrix region in Figure 8(e), the structure with the alternating appearance of positive and

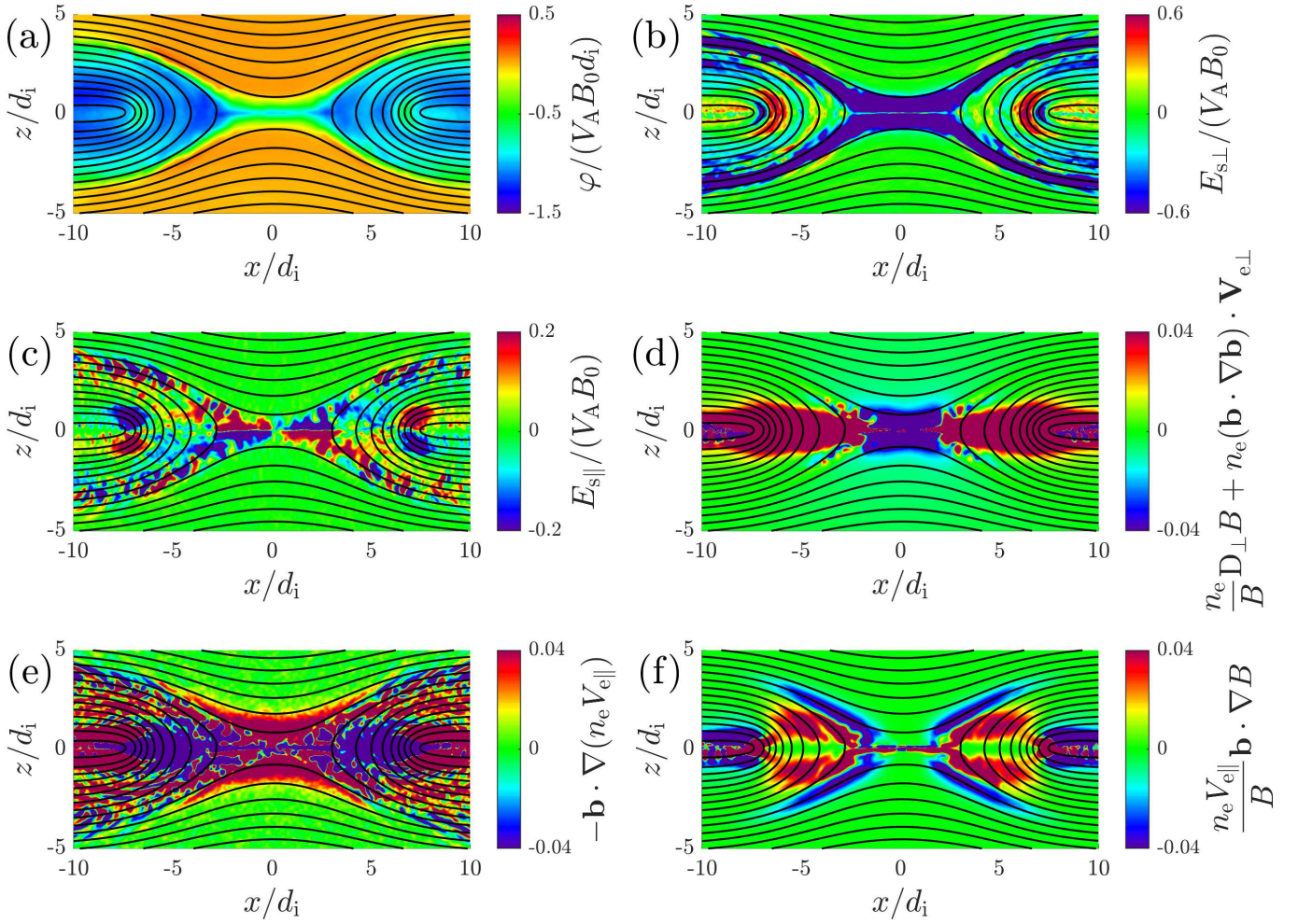


**Figure 8.** Color contours of (a) the electrostatic potential  $\varphi$ , (b) the perpendicular component of electrostatic field  $E_{s\perp}$ , (c) the parallel component of electrostatic field  $E_{s\parallel}$ , (d)  $\frac{n_e}{B} D_{\perp} B + n_e (\mathbf{b} \cdot \nabla \mathbf{b}) \cdot \mathbf{V}_{e\perp}$ , (e)  $-\mathbf{b} \cdot \nabla (n_e V_{e\parallel})$ , and (f)  $\frac{n_e V_{e\parallel}}{B} \mathbf{b} \cdot \nabla B$  at  $\Omega_{it} = 22.0$ . The black lines in the figure represent the magnetic field lines (Case B).

negative  $-\mathbf{b} \cdot \nabla (n_e V_{e\parallel})$  is also observed, which demonstrates that the charge separation associated with ESWs is driven by the term  $-\mathbf{b} \cdot \nabla (n_e V_{e\parallel})$  in Equation (1).

#### 4. Conclusions and Discussion

Using 2.5D PIC simulation, we investigated the formation of the charge separation in antiparallel magnetic reconnection. During the reconnection process, the charge separation is formed in three regions: the electron inflow region and the DF region both exhibit a positive charge density, while the electron outflow region exhibits a negative charge density. These charge separations generate the Hall electric field perpendicular to the magnetic field and the parallel electrostatic field. We quantitatively analyzed the effects of the magnetic flux tube's geometric dimensions and the parallel electron flux on the formation of charge separation. In the electron inflow region, the flux tube expands as it moves into the X-line, which contributes to a decrease in electron density. To balance the decrease in electron density, the parallel electron flux generates a net inflow of electrons. In this process, the electrons flow into the diffusion region along the flux tube, from regions with smaller cross sections to regions with larger cross sections, which contributes to a decrease in electron density near the separatrix. Finally, a positive charge

density is observed in the inflow region near the separatrix. In contrast to the inflow region, the outflow region features shrinking flux tube and parallel electron flux directed away from the diffusion region. This configuration leads to a negative charge density in the outflow region near the separatrix. Besides, we attribute the charge separation in the DF region mainly to the acceleration of electrons, which generates a sharply varying parallel electron flux. This pronounced  $-\mathbf{b} \cdot \nabla (n_e V_{e\parallel})$  drives a net outflow of electrons and establishes an accumulation of positive charge.

Compared to the mechanism proposed by J. Egedal et al. (2015), we introduced an equation to analyze the charge separation systematically, and we find the role of term  $\frac{n_e V_{e\parallel}}{B} \mathbf{b} \cdot \nabla B$  in Equation (1), which is responsible for the charge separation in the inflow and outflow regions near the separatrix. Besides, the development of the strong double layer is likely to be suppressed with a large  $\beta_{e\infty}$ , and a threshold  $\beta_{e\infty} < \sqrt{m_e/m_i}$  is given in J. Egedal et al. (2015). In our simulation, two cases configure with different values of  $\beta_{e\infty}$ —specifically, they are  $\beta_{e\infty} = 0.050 = \sqrt{m_e/m_i}$  in Case A and  $\beta_{e\infty} = 0.003 < \sqrt{m_e/m_i}$  in Case B. The magnitude of parallel electrostatic field  $E_{s\parallel}$  in Case A is much smaller than that in Case B, which demonstrates that the threshold  $\beta_{e\infty} < \sqrt{m_e/m_i}$

is a credible estimate. In this paper, we have studied the formation of the charge separation in antiparallel magnetic reconnection. However, the structure of Hall electric field in guide field magnetic reconnection will be distorted (S. Zenitani & M. Hoshino 2008; S. Fu et al. 2018; S. Lu et al. 2021), which indicates that the spatial distribution of charge separation is different from that in antiparallel magnetic reconnection. Therefore, the formation of the charge separation in guide field magnetic reconnection needs further study.

### Acknowledgments

This work was supported by the NSFC grants 42230201 and 42274196, the National Key Research and Development Program of China (No. 2022YFA1604600), and the Strategic Priority Research Program of the Chinese Academy of Sciences, grant No. XDB 41000000. The EPOCH code used in this work was in part funded by the UK EPSRC grants EP/G054950/1, EP/G056803/1, EP/G055165/1, EP/M022463/1, and EP/P02212X/1. The simulation data set is available in S. Hu (2025) with the URL doi:10.57760/sciencedb.space.02473.

### Appendix

#### Derivation of Equation (1)

Equation (1) is obtained through the simultaneous solution of the following equations:

$$\frac{\partial \mathbf{B}}{\partial t} = \nabla \times (\mathbf{V}_e \times \mathbf{B}), \quad (\text{A1})$$

$$\frac{\partial n_e}{\partial t} + \nabla \cdot (n_e \mathbf{V}_e) = 0, \quad (\text{A2})$$

where Equation (A1) is the induction equation for ideal electron fluid, which satisfies  $\mathbf{E} + \mathbf{V}_e \times \mathbf{B} = 0$ . Through vector calculation, Equation (A1) can be written as

$$\begin{aligned} \frac{\partial \mathbf{B}}{\partial t} = & (\nabla \cdot \mathbf{B}) \mathbf{V}_e - (\mathbf{V}_e \cdot \nabla) \mathbf{B} \\ & - (\nabla \cdot \mathbf{V}_e) \mathbf{B} + (\mathbf{B} \cdot \nabla) \mathbf{V}_e, \end{aligned} \quad (\text{A3})$$

where  $\nabla \cdot \mathbf{B} = 0$ . By taking the dot product with the unit magnetic field vector  $\mathbf{b}$  on both sides of Equation (A3) and scaling by  $1/B$ , we obtain

$$\begin{aligned} & \frac{1}{B} \left( \frac{\partial \mathbf{B}}{\partial t} + \mathbf{V}_e \cdot \nabla \mathbf{B} \right) \\ = & -\nabla \cdot \mathbf{V}_e - (\mathbf{b} \cdot \nabla \mathbf{b}) \cdot \mathbf{V}_e + (\mathbf{b} \cdot \nabla) V_{e\parallel}, \end{aligned} \quad (\text{A4})$$

where  $V_{e\parallel} = \mathbf{b} \cdot \mathbf{V}_e$ . Meanwhile, Equation (A2) can be written as

$$\left( \frac{\partial n_e}{\partial t} + \mathbf{V}_e \cdot \nabla n_e \right) = -n_e \nabla \cdot \mathbf{V}_e. \quad (\text{A5})$$

By combining Equations (A4) and (A5) through elimination of the term  $\nabla \cdot \mathbf{V}_e$ , we derive

$$\begin{aligned} & \left( \frac{\partial n_e}{\partial t} + \mathbf{V}_e \cdot \nabla n_e \right) \\ = & \frac{n_e}{B} \left( \frac{\partial \mathbf{B}}{\partial t} + \mathbf{V}_e \cdot \nabla \mathbf{B} \right) \\ & + n_e (\mathbf{b} \cdot \nabla \mathbf{b}) \cdot \mathbf{V}_e - n_e (\mathbf{b} \cdot \nabla) V_{e\parallel}. \end{aligned} \quad (\text{A6})$$

Substituting the velocity decomposition  $\mathbf{V}_e = V_{e\parallel} \mathbf{b} + \mathbf{V}_{e\perp}$  into Equation (A6), we derive

$$\begin{aligned} D_{\perp} n_e = & \frac{n_e}{B} D_{\perp} \mathbf{B} + n_e (\mathbf{b} \cdot \nabla \mathbf{b}) \cdot \mathbf{V}_{e\perp} \\ & - \mathbf{b} \cdot \nabla (n_e V_{e\parallel}) + \frac{n_e V_{e\parallel}}{B} \mathbf{b} \cdot \nabla \mathbf{B}, \end{aligned} \quad (\text{A7})$$

where  $D_{\perp} = \left( \frac{\partial}{\partial t} + \mathbf{V}_{e\perp} \cdot \nabla \right)$  and  $(\mathbf{b} \cdot \nabla \mathbf{b}) \cdot \mathbf{V}_{e\perp} = (\mathbf{b} \cdot \nabla \mathbf{b}) \cdot \mathbf{V}_e$ . Equation (A7) coincides with Equation (1).

### ORCID iDs

Shihang Hu  <https://orcid.org/0009-0000-9423-5131>  
 Quanming Lu  <https://orcid.org/0000-0003-3041-2682>  
 Yukang Shu  <https://orcid.org/0000-0003-0691-1596>  
 San Lu  <https://orcid.org/0000-0003-2248-5072>  
 Kai Huang  <https://orcid.org/0000-0003-3630-309X>  
 Jia Nan  <https://orcid.org/0000-0001-8033-2336>

### References

- Arber, T. D., Bennett, K., Brady, C. S., et al. 2015, *PPCF*, **57**, 113001  
 Birn, J., Drake, J. F., Shay, M. A., et al. 2001, *JGRA*, **106**, 3715  
 Biskamp, D. 2000, *Magnetic Reconnection in Plasmas*, Cambridge Monographs on Plasma Physics (Cambridge: Cambridge Univ. Press), doi:10.1017/CBO9780511599958  
 Cassak, P. A., & Shay, M. A. 2012, *SSRv*, **172**, 283  
 Chang, C., Huang, K., Lu, Q., et al. 2021, *JGRA*, **126**, e2021JA029290  
 Dahlin, J. T., Drake, J. F., & Swisdak, M. 2014, *PhPI*, **21**, 092304  
 Dong, Q.-L., Wang, S.-J., Lu, Q.-M., et al. 2012, *PhRvL*, **108**, 215001  
 Drake, J. F., Shay, M. A., & Swisdak, M. 2008, *PhPI*, **15**, 042306  
 Egedal, J., Daughton, W., Le, A., & Borg, A. L. 2015, *PhPI*, **22**, 101208  
 Egedal, J., Fox, W., Katz, N., et al. 2007, *PhRvL*, **98**, 015003  
 Fu, H. S., Chen, F., Chen, Z. Z., et al. 2020, *PhRvL*, **124**, 095101  
 Fu, H. S., Khotyaintsev, Y. V., André, M., & Vaivads, A. 2011, *GeoRL*, **38**, L16104  
 Fu, H. S., Khotyaintsev, Y. V., Vaivads, A., André, M., & Huang, S. Y. 2012, *GeoRL*, **39**, L06105  
 Fu, H. S., Khotyaintsev, Y. V., Vaivads, A., Retinò, A., & André, M. 2013, *NatPh*, **9**, 426  
 Fu, S., Huang, S., Zhou, M., Ni, B., & Deng, X. 2018, *AnGeo*, **36**, 373  
 Fujimoto, K. 2014, *GeoRL*, **41**, 2721  
 Goldman, M. V., Newman, D. L., & Lapenta, G. 2016, *SSRv*, **199**, 651  
 Gosling, J. T., Skoug, R. M., McComas, D. J., & Smith, C. W. 2005, *JGRA*, **110**, A01107  
 Hu, S. 2025, The Data of the Article ‘‘Electrostatic Field Formed by Charge Separation in Anti-parallel Magnetic Reconnection’’, doi:10.57760/sciencedb.space.02473  
 Huang, C., Lu, Q., Wang, P., Wu, M., & Wang, S. 2014, *JGRA*, **119**, 6445  
 Huang, C., Wang, R., Lu, Q., & Wang, S. 2010, *ChSBu*, **55**, 718  
 Huang, C., Wu, M., Lu, Q., Wang, R., & Wang, S. 2015, *JGRA*, **120**, 1759  
 Huang, K., Lu, Q., Lu, S., Wang, R., & Wang, S. 2021, *JGRA*, **126**, e2021JA029939  
 Karimabadi, H., Daughton, W., & Scudder, J. 2007, *GeoRL*, **34**, L13104  
 Krucker, S., Hudson, H. S., Glesener, L., et al. 2010, *ApJ*, **714**, 1108  
 Li, C. K., Séguin, F. H., Frenje, J. A., et al. 2007, *PhRvL*, **99**, 055001  
 Lu, Q., Fu, H., Wang, R., & Lu, S. 2022, *ChPhB*, **31**, 089401  
 Lu, Q., Huang, C., Xie, J., et al. 2010, *JGRA*, **115**, A11208  
 Lu, Q., Wang, R., Xie, J., et al. 2011, *ChSBu*, **56**, 1174  
 Lu, S., Angelopoulos, V., & Fu, H. 2016, *JGRA*, **121**, 9483  
 Lu, S., Angelopoulos, V., Pritchett, P. L., et al. 2021, *JGRA*, **126**, e2021JA029550  
 Lu, S., Artemyev, A. V., Angelopoulos, V., Pritchett, P. L., & Runov, A. 2019, *GeoRL*, **46**, 28  
 Ma, Z. W., & Bhattacharjee, A. 2001, *JGRA*, **106**, 3773  
 Masuda, S., Kosugi, T., Hara, H., Tsuneta, S., & Ogawara, Y. 1994, *Natur*, **371**, 495  
 Øieroset, M., Phan, T. D., Fujimoto, M., Lin, R. P., & Lepping, R. P. 2001, *Natur*, **412**, 414  
 Pritchett, P. L. 2001, *JGRA*, **106**, 3783  
 Runov, A., Angelopoulos, V., Zhou, X.-Z., et al. 2011, *JGRA*, **116**, A05216  
 Sang, L., Lu, Q., Xie, J., et al. 2022, *PhPI*, **29**, 102108

- Shay, M. A., Drake, J. F., Rogers, B. N., & Denton, R. E. 2001, *JGRA*, **106**, 3759
- Vasyliunas, V. M. 1975, *RvGeo*, **13**, 303
- Wang, H., Lu, Q., Huang, C., & Wang, S. 2016, *ApJ*, **821**, 84
- Wang, R., Cheng, Z., Slavin, J. A., et al. 2024, *GeoRL*, **51**, e2023GL106282
- Wang, R., Du, A., Nakamura, R., et al. 2013, *GeoRL*, **40**, 2511
- Wang, R., Lu, Q., Du, A., & Wang, S. 2010, *PhRvL*, **104**, 175003
- Wang, R., Lu, Q., Khotyaintsev, Y. V., et al. 2014, *GeoRL*, **41**, 4851
- Wang, R., Wang, S., Lu, Q., et al. 2023a, *NatAs*, **7**, 18
- Wang, R., Yu, X., Wang, Y., Lu, Q., & Lu, S. 2023b, *ApJ*, **947**, 78
- Wang, S., & Lu, Q. 2019, *Collisionless Magnetic Reconnection* (Beijing: Science Press)
- Wang, Z., Vaivads, A., Fu, H. S., et al. 2023, *ApJ*, **946**, 67
- Wei, F., Hu, Q., Feng, X., & Fan, Q. 2003, *SSRv*, **107**, 107
- Wu, M., Lu, Q., Volwerk, M., et al. 2013, *JGRA*, **118**, 4804
- Wu, P., Shay, M. A., Phan, T. D., Oieroset, M., & Oka, M. 2011, *PhPI*, **18**, 111204
- Wygant, J. R., Cattell, C. A., Lysak, R., et al. 2005, *JGRA*, **110**, A09206
- Yamada, M., Kulsrud, R., & Ji, H. 2010, *RvMP*, **82**, 603
- Yamada, M., Ren, Y., Ji, H., et al. 2006, *PhPI*, **13**, 052119
- Yamada, M., Yoo, J., Jara-Almonte, J., et al. 2015, *PhPI*, **22**, 056501
- Zenitani, S., & Hoshino, M. 2008, *ApJ*, **677**, 530
- Zhang, T. L., Lu, Q. M., Baumjohann, W., et al. 2012, *Sci*, **336**, 567
- Zhou, M., Deng, X. H., Zhong, Z. H., et al. 2019, *ApJ*, **870**, 34